J A C S
JOURNAL OF THE AMERICAN CHEMICAL SOCIETY
pubs.acs.org/JACS
Article

Fjord-Edge Graphene Nanoribbons with Site-Specific Nitrogen Substitution

Yolanda L. Li, Chih-Te Zee, Janice B. Lin, Victoria M. Basile, Mit Muni, Maria D. Flores, Julen Munárriz, Richard B. Kaner, Anastassia N. Alexandrova, K. N. Houk, Sarah H. Tolbert, and Yves Rubin*

Cite This: *J. Am. Chem. Soc.* 2020, 142, 18093−18102
Read Online

ACCESS | Metrics & More | Article Recommendations | Supporting Information

ABSTRACT: The synthesis of graphene nanoribbons (GNRs) that contain site-specifically substituted backbone heteroatoms is one of the essential goals that must be achieved in order to control the electronic properties of these next generation organic materials. We have exploited our recently reported solid-state topochemical polymerization/cyclization-aromatization strategy to convert the simple 1,4-bis(3-pyridyl)butadiynes **3a,b** into the fjord-edge nitrogen-doped graphene nanoribbon structures **1a,b** (fjord-edge $N_2[8]$GNRs). Structural assignments are confirmed by CP/MAS ^{13}C NMR, Raman, and XPS spectroscopy. The fjord-edge $N_2[8]$GNRs **1a,b** are promising precursors for the novel backbone nitrogen-substituted $N_2[8]_A$GNRs **2a,b**. Geometry and band calculations on $N_2[8]_A$GNR **2c** indicate that this class of nanoribbons should have unusual bonding topology and metallicity.

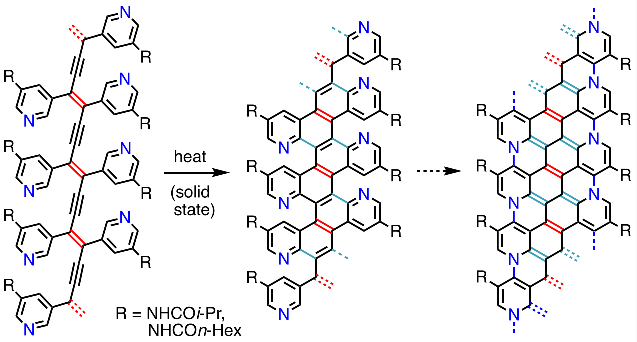

INTRODUCTION

Graphene nanoribbons (GNRs) are expected to usher in the ultimate nanosizing of electronics[1−4] and sensors[5,6] for next generation devices. The electronic properties of GNRs can be exquisitely tuned by modification of their width, backbone, and edge structure.[1,7−10] In the past decade, both on-surface and in-solution bottom-up syntheses have achieved precise structural control over these benchmarks.[11−15] Early bottom-up syntheses have focused on GNRs with armchair[16−20] or zigzag[21] edges. More recently, intricate edge or interior configurations, such as chevron,[11,22−24] cove,[25−27] fjord,[28] or holey,[29−31] have been obtained. These novel topologies significantly alter the electronic or magnetic properties of GNRs, as do atomically precise[32] substitutions of carbons with heteroatoms such as boron,[33,34] sulfur,[35,36] or nitrogen.[30,37,38] Crucially, site-specific doping at the GNR *backbone* produces a dramatic alteration of its electronics, making such structures the most desirable targets for synthesis.[32,39−41] Nitrogen doped GNRs are of particular interest as they produce p-doped materials.[24,37,38,42−45]

Herein, we describe the synthesis of the first eight-atom wide, fjord-edge nitrogen-doped graphene nanoribbons (fjord-edge $N_2[8]$GNRs **1a,b**; Figure 1). Fjord-edge $N_2[8]$GNRs **1a,b** were obtained in a facile two-step conversion starting from dipyridyl diynes **3a,b**. Photochemically induced topochemical polymerization in the crystalline state afforded polydiacetylenes (PDAs) **4a,b**, which were thermally converted to GNRs **1a,b** with no loss of the side chains. The Hopf cyclization and ensuing aromatization from PDAs **4a,b** to GNRs **1a,b** was monitored by cross-polarization magic angle spinning (CP/MAS) solid state ^{13}C NMR. X-ray photoelectron spectroscopy (XPS) revealed both the pyridinic and amide bonding states of the nitrogen atoms. Raman spectroscopy further confirmed the structural integrity of the fjord-edge $N_2[8]$GNRs **1a,b**.

RESULTS AND DISCUSSION

Diyne Monomer Synthesis. The topochemical polymerization of diynes requires suitable packing of the monomers in the crystal to trigger subsequent chain reactions.[46−48] Here, the dipyridyl diyne units of **3a,b,d** (Scheme 1, Figure 1) needed to have the diyne 1,4′-carbons within van-der-Waals contact distance (∼3.5 Å) to promote facile formation of intermolecular bonds, a process that often occurs under ambient light.[49,50] Although we synthesized several isomeric dipyridyl diyne systems,[51] only one series, based on 3-amino-5-alkynylpyridine, gave the polymerizable diynes **3a,b**. Accordingly, 3-amino-5-bromopyridine was coupled with trimethylsilylacetylene under Sonogashira conditions, followed by

Received: July 16, 2020
Published: September 8, 2020

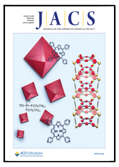

https://dx.doi.org/10.1021/jacs.0c07657
J. Am. Chem. Soc. 2020, 142, 18093−18102

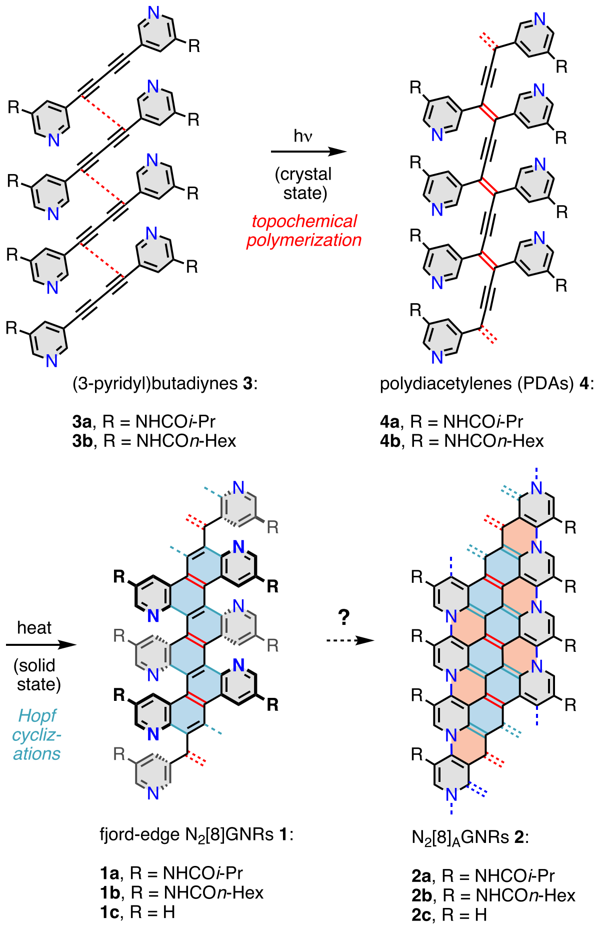

Figure 1. Synthesis of fjord-edge nitrogen-doped graphene nanoribbons (fjord-edge N$_2$[8]GNRs **1a**,**b**).

Scheme 1. Synthesis of the 1,4-Bis(3-pyridyl)butadiynes 3a,b,d.

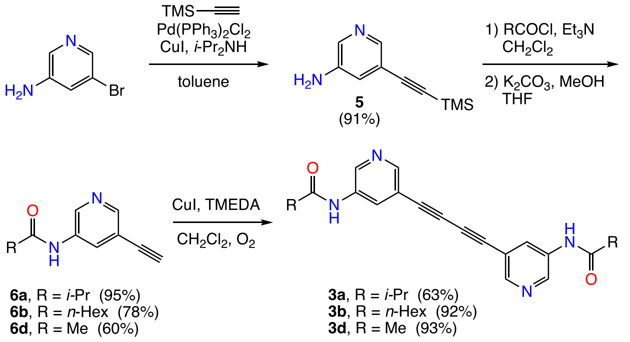

acylation of amine **5** with the corresponding acid chlorides (Scheme 1, R = *i*-Pr, *n*-Hex, Me). Removal of the trimethylsilyl protecting group gave alkynyl amides **6a**,**b**,**d** in good to excellent yields. Oxidative coupling under the Hay conditions afforded diyne amides **3a**,**b**,**d** in good to high yields.

X-ray Structure. Crude diyne **3a** afforded single crystals after slow evaporation from methanol (Figure S28a,b).[51] X-ray diffraction at the Advanced Photon Source (APS) of the Argonne National Lab (Figure S29) afforded a 1.0 Å resolution crystal structure of diyne **3a** (Figure 2, Table S1).[51]

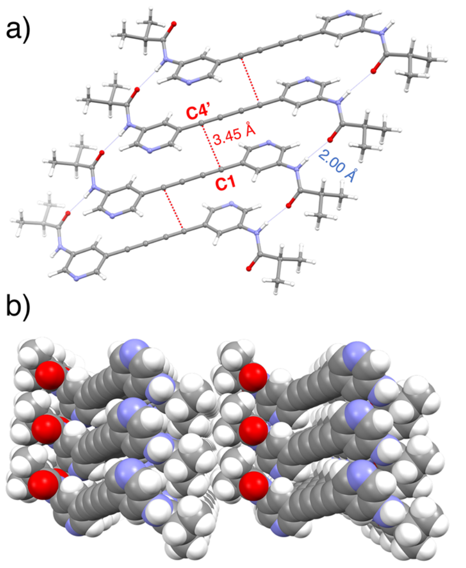

Figure 2. (a) Crystal packing structure for diyne **3a** displaying the short C1−C4' distance directed by the C=O···H−N hydrogen-bonded network. (b) View of **3a** down the H-bonding axis.

The crystal packing geometry for molecules of diyne **3a** validates the desired short, nonbonded C1−C4' distance of 3.45 Å (Figure 2a). The hydrogen bonds between the carbonyl oxygens and amide hydrogens have an optimal distance of 2.00 Å, guiding the assembly of diyne units in **3a** along the unit cell vector *a*. The relative strength of these intermolecular interactions is reflected in the crystal morphology and powder diffraction (Figures S28 and S30). To accommodate the H-bonding motif, the polymer growth axis exhibits a horizontal offset between each molecule, organizing the diynes into an optimal arrangement for topochemical polymerization (Figure 2b). While we were not able to obtain the single crystal structure of **3b**, its powder diffraction displayed a similar packing arrangement to **3a** (Figure S31).

Topochemical Polymerization of Diynes 3a,b. Both dipyridyl diynes **3a**,**b** quickly polymerized to dipyridyl PDAs **4a**,**b** when subjected to UV light, as well as under ambient light, whereas diyne **3c** was unreactive. The polymerizations were carried out by the irradiation of finely pulverized dispersions of the crystals in hexanes using a medium pressure Hanovia lamp (Pyrex filter), typically for 12 h, producing a deep purple/black material. Dissolution of unreacted monomer from the polymerized crystals gave the nearly insoluble, pristine polydiacetylenes **4a**,**b** (18 and 4%, respectively) as fibrous powders after filtration. The low polymerization yield for **3b** appears to be inherent to this derivative, since repeated attempts to increase yields by using nanocrystalline material could not raise the conversion yield for this substrate.

Conversion of PDAs 4a,b to GNRs 1a,b. Thermal conversion experiments were carried out in separate runs on PDAs **4a**,**b** under increasingly higher temperatures in argon.[51] This transformation could be conveniently monitored by CP/MAS ^{13}C solid state NMR, focusing on the four distinct carbon signal ranges corresponding to the four functional groups of interest (Figure 3b,c): amide carbonyls (160−170 ppm), aromatic carbons (110−150 ppm), alkynyl carbons (∼100 ppm), and amide side chains (10−40 ppm). As the PDAs **4a**,**b** were heated under increasingly higher temperatures (1h each per run), the distinct ^{13}C NMR signals tracked an initial Hopf cyclization, as evidenced by the disappearance of the alkyne peak at temperatures between 300 and 350 °C (Figure 3b,c). Thus, the Hopf cyclization reactions of PDAs **4a**,**b** occur more

https://dx.doi.org/10.1021/jacs.0c07657
J. Am. Chem. Soc. 2020, 142, 18093−18102

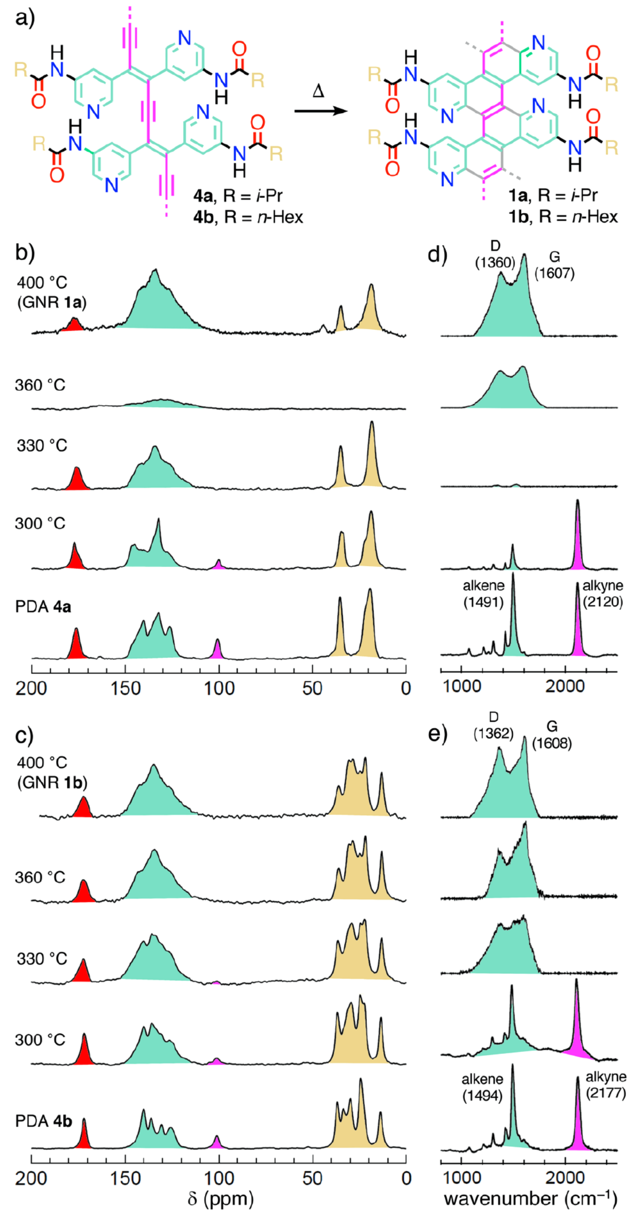

Figure 3. CP/MAS solid-state ^{13}C NMR and Raman spectra for the products obtained by heating PDAs **4a,b**. Each heating experiment was carried out for 1 h using a fresh sample of PDA. (a) PDAs **4a,b** and GNRs **1a,b** are color-coded by chemical shift region to reflect spectral changes in parts b and c. (b) PDA **4a** conversion to fjord-edge N$_2$[8]GNR **1a**, and (c) PDA **4b** conversion to fjord-edge N$_2$[8]GNR **1b**. The very broad, weak signal for the sample heated at 360 °C in part b is due to an air-stable π-radical intermediate formed during heating.[52] Baseline-corrected Raman spectra for the conversion of (d) PDA **4a** to fjord-edge N$_2$[8]GNR **1a**, and (e) PDA **4b** to fjord-edge N$_2$[8]GNR **1b**. The very weak Raman signal for the sample heated at 330 °C in part d is due to the strong background fluorescence of this sample, which was smoothed out through baseline correction.

readily, ~100 °C lower than for our phenyl analogs.[50] The Hopf cyclization step is followed by further aromatization reactions that form fjord-edge N$_2$[8]GNRs **1a** and **1b** at temperatures between 350 and 400 °C (Figure 3b,c), as revealed by the changes in the overall envelope for the aromatic signals between 110−150 ppm, which adopt an underlying intensity ratio of 1:2:1 for both **1a** and **1b** (Figure 3b,c, Table 1a). Curve fitting of the experimental spectrum of **1b** in the 110−150 ppm range with seven Gaussian curves of equal intensity and width, representing the expected number of aromatic ^{13}C signals for fjord-edge N$_2$[8]GNR **1b**, affords the fitted peaks in Table 1. These values compare rather well with the calculated values for model compound **1e** (Table 1b, top). Furthermore, the clusters of peaks for the aromatic carbons for each of the alternate possible model structures, i.e., **7c** and **8c** (Table 1b, middle and bottom), which are the structural alternatives in the conversion of polydiacetylenes **4a,b** to fjord-edge N$_2$[8]GNRs **1a,b** (see discussion below and Figure 5), do not fit the experimental curve as well. In particular, structure **7c** has its A,B peaks clustered around 144 ppm, which leaves a large empty void between these peaks and the C−G peaks. This gap is even wider for structure **8c**, which has a ~20 ppm gap between the clusters of A,B and C−G peaks. Thus, the experimental CP/MAS ^{13}C solid state NMR spectrum of fjord-edge N$_2$[8]GNR **1b** matches best the calculated chemical shifts of model structure **1e**.

Furthermore, the convergence of both PDAs **4a** and **4b** to identical aromatic peak shapes upon heating indicates that they both likely undergo similar processes to form the same fjord-edge N$_2$[8]GNR core. Subsequent heating of **4a** and **4b** to temperatures as high as 400 °C shows no change in the ^{13}C CP/MAS spectra, suggesting that the fjord-edge N$_2$[8]GNRs **1a,b** have fully formed at 330 and 360 °C. These lower conversion temperatures prevent side chain fragmentation, unlike in our previous work on [8]$_A$GNR, which required temperatures as high as 500 °C for full conversion.[50]

As expected, the presence of side chains in fjord-edge N$_2$[8]GNRs **1a,b** increases their solubility to a small extent: sonication in strongly hydrogen-bonding *N*-methyl-2-pyrrolidone (NMP), followed by filtration through a 0.2 μm Teflon membrane, gives yellowish solutions of fjord-edge N$_2$[8]GNRs **1a,b** (UV−vis, see Figure S27).[51]

Raman Spectroscopy. The precursor PDAs **4a,b** both exhibit strong alkene peaks at 1494 and 1491 cm^{-1}, respectively, as well as alkyne peaks at 2117 and 2120 cm^{-1}, respectively, which are typical of the enyne backbone (Figure 3d,e, bottom traces). Upon heating, these signals disappear, while the signature D and G peaks of GNRs **1a,b** appear (Figure 3d,e, top traces). The Raman spectra for fjord-edge N$_2$[8]GNRs **1a,b** show D peaks at 1360 and 1362 cm^{-1}, and G peaks at 1607 and 1608 cm^{-1}, respectively. The G peaks of these GNRs are upshifted by ~30 cm^{-1} from graphene (1580 cm^{-1}), due to the confined, strongly aggregated nature of GNRs **1a,b** (see HR-TEM imaging, Figure S32).[51] Prior reports on GNRs show similar shifts in the D peak as well.[53] Furthermore, the broad feature of the observed D peaks can be attributed to the fjord-edge structure and the high levels of site-specific heteroatom substitutions, as noted below.

Broadening of the D peak is generally caused by defects within the graphene lattice.[54−56] The fjord-edge GNRs **1a,b** have two inherent structural features that broaden the D peak beyond previously reported GNR examples. Specifically, fjord-edges represent bond vacancies along the edges of pristine graphene. Broad D and G peaks are characteristic of a large numbers of defects, which can also be seen in the all-carbon fjord edge [8]GNR.[28] Further broadening of the D peaks is caused by distortion of the lattice from the nitrogen dopant. Reports for both nitrogen doped graphene and top-down synthesized doped GNRs have shown broad D peaks with various levels of dopant atoms.[57,58] The bottom-up approach

Table 1. Comparison of (a) the Curve-Fitted Experimental[a] Spectrum of Fjord-Edge N_2[8]GNR 1b, and (b) Calculated ^{13}C NMR Chemical Shifts for Model Structures 1e, 7c, and 8c.[51]

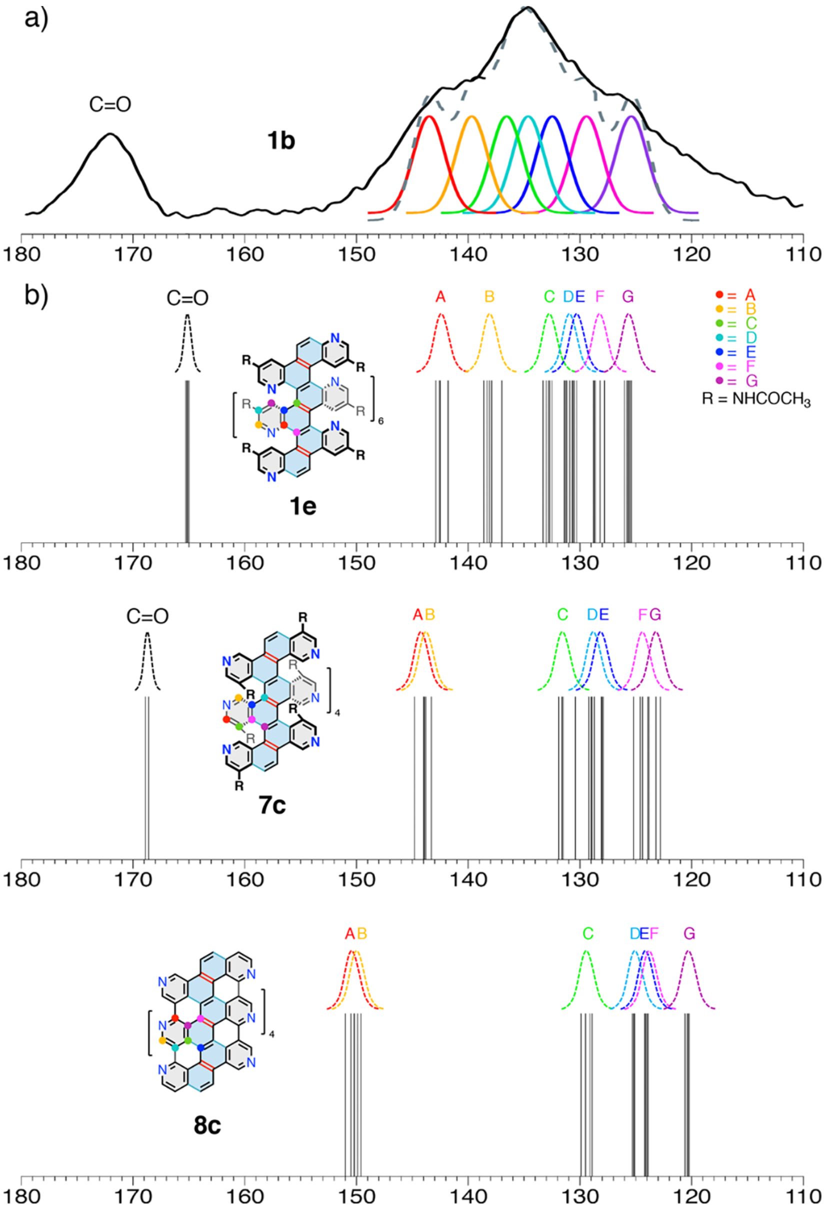

Carbon	A	B	C	D	E	F	G
Fitted δ^a	143.5	139.7	136.5	134.5	132.5	129.4	125.4
1e, calc $\delta^{b,c}$	142.6	138.0	132.9	131.3	130.6	128.5	125.7
7c, calc $\delta^{b,c}$	144.0	143.6	131.6	129.4	128.2	124.4	123.6
8c, calc $\delta^{b,c}$	150.3	150.0	129.4	125.2	124.1	124.0	120.4

[a]The experimental CP/MAS ^{13}C NMR spectrum is plotted as a solid black line, while the sum of the curve fits is a gray dashed line. [b]Average of the DFT calculated chemical shifts (GIAO/B3LYP//6-31G(d)) for each of the seven distinct, nonsymmetrically related carbons defined in part b). Gaussian curves of arbitrary but constant width and height are displayed for better visualization of the groups of chemical shifts belonging to each of the seven types of nonsymmetrically related carbons for each structure. [c]See Figures S39−S41.

of our synthesis incorporates higher levels of nitrogen doping, 10% by atom (based on core aromatic ring C,N,H atoms only), which likely further accounts for the broad D peak.[59]

XPS Spectra. To confirm the formation of a fjord-edge topology in compounds **1a,b**, we examined the nitrogen bonding environment present in GNRs **1a,b** using XPS spectroscopy (Figure 4). GNRs **1a,b** should contain solely pyridinic and amide nitrogens if the fjord edge structure is exclusively formed. As expected, the XPS spectra of GNRs **1a,b** show signatures corresponding to the pyridinic[60,61] (398.7 eV) and amide[62] (399.7 eV) bonding, and no other species (Figure 4). Notably, we do not see the presence of internal graphitic (401.7 eV)[60,61,63,64] or pyridinium species (402.5 eV),[65,66] which would indicate further cyclizations have occurred beyond the fjord edge structure (see discussion below and Figure 5). Additionally, the retention of the side chain substituents indicates that the alternate path of cyclization to an edge-like topology (**8**), via intermediates **7a,b** (Figures 5

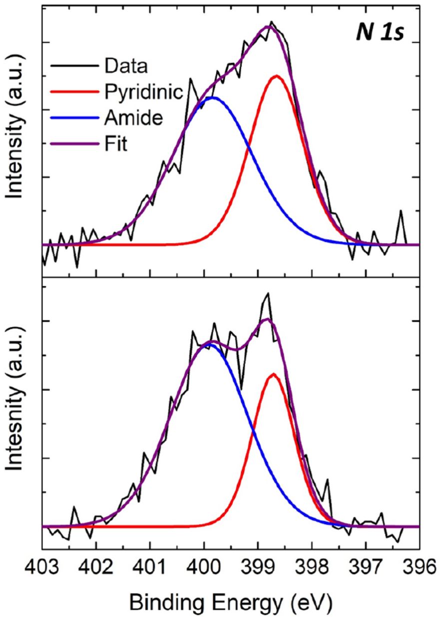

Figure 4. N 1s XPS spectra for fjord-edge N_2[8]GNR **1a** and **1b**, with pyridinic and amide nitrogens centered at 398.7 and 399.7 eV, respectively.

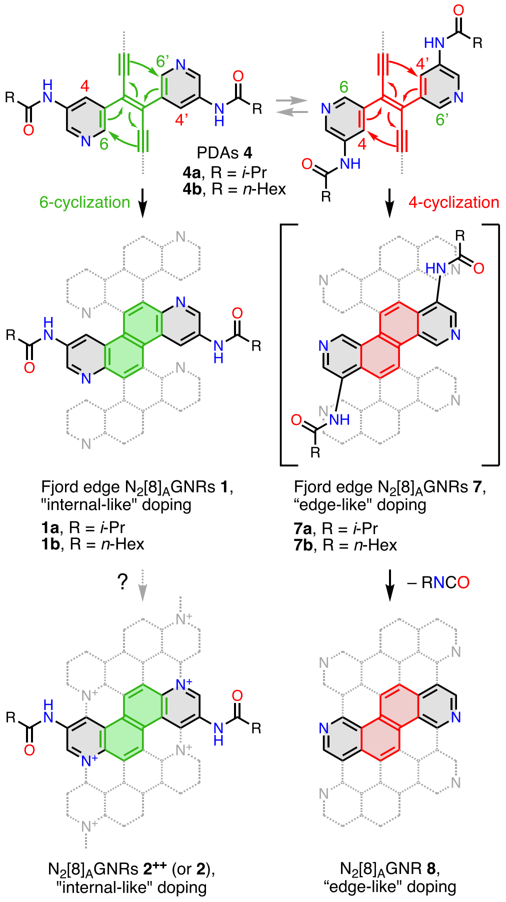

Figure 5. Two Hopf cyclization pathways for PDAs **4a,b**, which can occur at either the 4 or 6-positions of the pyridyl rings, resulting in the nitrogen atoms being located at either internal (**1a,b** or **2,2**$^{++}$) or at edge locations (**7a,b** or **8**).

and 6), is unlikely to have occurred, in agreement with the calculations, which show this pathway to be highly unfavorable (see below). The increased width of the amide peak relative to the pyridinic peak is consistent with conformational disorder in the side-chains only. Together, these results all indicate that the structure most consistent with the data is that of the fjord-edge N_2[8]GNRs **1a,b**.

Conformation Preference, Cyclization Pathways, and Reaction Barriers. The conformational preference in a model system for the fjord-edge N_2[8]GNR **1**, R = NHCOMe) was investigated with its two extreme cases, all-zigzag and helical (see Section S4.8).[51] The fjord edge structure of **1a,b** imparts strong steric repulsion between the pyridine nitrogen lone pairs and the C−H bonds of adjacent diazachrysene units. Thus, the two possible key conformations, all-zigzag (alternating up−down pyridyl units) and helical (all pyridyl units staggered in a nonalternating fashion) were calculated at the semiempirical (PM3) and DFT (B3LYP) levels. The differences in energy (35.9 and 60.2 kcal·mol^{-1} for PM3 and B3LYP, respectively) between the two conformers is very high, thus it is likely that only the zigzag conformation exists in the fjord-edge N2[8]GNRs **1a,b** as represented in Figure 1.

There are two possible Hopf cyclization pathways for PDAs **4a,b** (Figure 5), which can afford fjord-edge GNRs with two different topologies. The internal-like topology (**1a,b**) has the nitrogen atoms opposite to C−H bonds of the next "diazachrysene" units, while the edge-like topology has them at the edges of the fjord-edge nanoribbons **7a,b**, or the ensuing $N_2[8]_A$GNR **8**, since it can be expected that the amide side chains should be easily lost from structure **7a,b** under our heating conditions. Unlike our previous work on $[8]_A$GNR,[50] which forms the same structure regardless of the initial cyclization pathway at the 2 or 4-positions of the PDAs' *m*-amidophenyl rings owing to subsequent thermally induced loss of sidechains, cyclization at either the similarly related 4 or 6-positions of the pyridyl rings in PDAs **4a,b** could give two different fjord-edge GNRs or a statistical mixture alternating both pathways along the nanoribbon length. However, cyclization at the 4-position should be strongly disfavored owing to the severe steric clash between the amide groups and adjacent pyridyl units during Hopf cyclization (structures **7a,b**, Figure 5). Furthermore, aromatization to the edge-doped armchair $N_2[8]_A$GNR **8** should easily ensue if the edge-like pathway is followed, resulting in total loss of the side chains. This is not the case, based on our experimental data (CP/MAS solid-state ^{13}C NMR and XPS, Figures 3 and 4). In fact, cyclization appears to favor the 6-position, which produces the lesser strained, internally doped fjord-edge N_2[8]GNRs **1a,b** with their amide side chains pointing away from the series of fused diazachrysene units. The transition state calculations reported below lend further strong support for the fact that the Hopf cyclization occurs at the 6-pyridyl positions to yield fjord-edge N_2[8]GNRs **1a,b**.

To further understand the energetics and pathway of the Hopf cyclization of PDAs **4a,b**, we base our theoretical considerations on previous results by Prall *et al.*[67] and our own work.[50] The Hopf cyclization mechanism has been calculated to proceed through an initial 6π-electrocyclization, followed by two consecutive [1,2]-H shifts, with the first H-shift as the rate-determining step.[68] As discussed above (Figure 5), the enediyne units of PDAs **4a,b** can undergo cyclization at either the 6-position (*para* to the amide group) or the 4-position (*ortho* to the amide group), the latter of which is intuitively

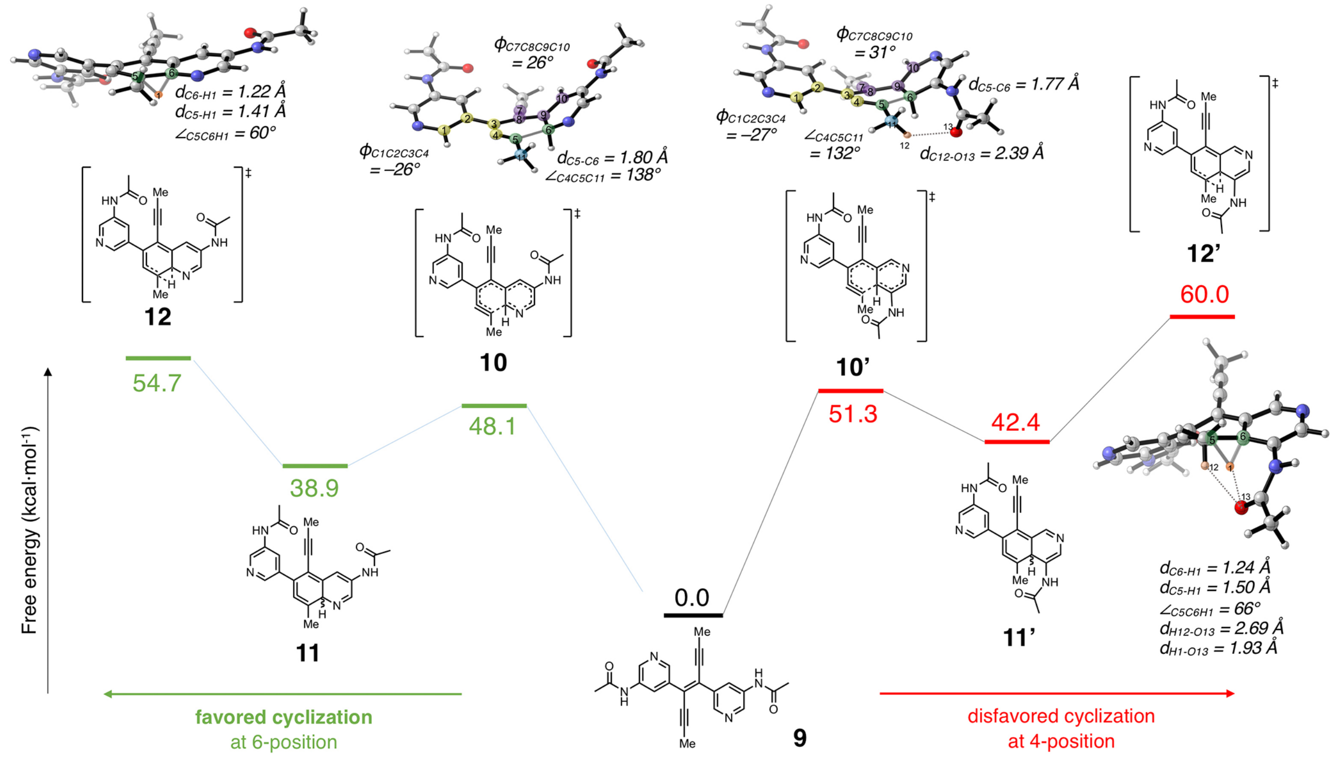

Figure 6. Free energies (in kcal·mol^{-1}) of the intermediates and transition states for both the favored (left) and disfavored (right) Hopf cyclization pathways relative to starting structure **9**.

unfavorable due to the large steric bulk of the amide group, compared to only H in **1a,b** (Figure 5).

Using density functional theory (DFT), we computed the geometries of the model system **9** (Figure 6), the transition states for the initial 6π electrocyclizations (**10** and **10'**), the strained allene intermediates **11** and **11'**, and the transition states for the rate-determining 1,2-shifts (**12** and **12'**). These structures were optimized in the gas-phase using B3LYP/6-31G(d), and single-point energy calculations were performed using M06-2*X*/6-311+G(d,p) with B3LYP frequencies to obtain free energy values. The potential energy surfaces for the two cyclization pathways are shown in Figure 6.

The energetic trends for this bispyridyl system are similar to the all-carbon system previously studied by us.[50] As expected, the barriers for cyclization at the 4-position are higher than those at the 6-position. The activation free energies for the more favorable transition states **10** and **12** are 48.1 and 54.7 kcal·mol^{-1}, respectively, while the analogous transition states **10'** and **12'** have higher barriers of 51.3 and 60.0 kcal·mol^{-1}, respectively. Like the all-carbon PDAs previously studied, the 1,2-shift following electrocyclization is the rate-determining step in both pathways, and the preference for the pathway with cyclization at the 6-position is substantial (5.3 kcal·mol^{-1}). This energy difference virtually ensures that the analogous series of cyclizations within PDAs **4a,b** should occur exclusively at the 6-positions (*para* to the amide group) of the pyridyl rings.

The geometries of the transition states **10** and **10'** are similar to each other and to their all-carbon variants. In **10** and **10'**, the π-system of the alkynes is planar, while the flanking pyridyl groups are out-of-plane by approximately 30°. The slightly higher barrier of **10'** is likely due to the close proximity of the amide oxygen and methyl group on the forming C−C bond. More ample differences can be seen between the rate-determining states **12** and **12'**. In **12**, the quinoline intermediate is planar, and the C6−H1 bond stretches to 1.22 Å from its normal C−H bond length of 1.09 Å. However, in the less-favorable transition state **12'**, the bulky amide group forces the quinoline out of plane, largely due to unfavorable steric interactions between the amide oxygen and the shifting hydrogen and adjacent methyl group, which accounts for the intrinsic preference for the 6-position cyclization.

Calculations for the unsubstituted variant (no amide groups) were also computed to probe the intrinsic preference for the 6-position (Figure S35).[51] The barriers of the rate-determining 1,2-shift for the unsubstituted system are 53.7 and 55.7 kcal·mol^{-1} for the 6 and 4-positions, respectively, with less strong of a preference (2.0 kcal·mol^{-1}) for the 6-position. Thus, the increased preference for the 6-position in the substituted system **9** can be wholly attributed to the unfavorable steric interactions between substituents in the rate-determining transition state structure **12'**.

We note that the barrier of the rate-determining step in pyridyl system **9** is ∼3 kcal·mol^{-1} lower than that of the all-carbon system, which correlates well with the ∼100 °C lower conversion temperature for this N-based system.

Electronic Properties of Fully Cyclized $N_2[8]_A$GNR. In order to better understand the electronic properties of the fully cyclized (graphitic) $N_2[8]_A$GNR system **2c**, we calculated the electronic Density of States (DOS) for the parent systems **1c** and **2c** by means of periodic DFT (Figures 1 and 7).[51] The DOS of **1c** and **2c**, obtained from the HSE06 functional on the basis of PBE geometries,[68,69] are depicted in Figure 7. As we can see, fjord-edge $N_2[8]$GNR **1c** is expected to be a semiconductor, with a bandgap of 2.04 eV (Figure 7a). Fully cyclized $N_2[8]_A$GNR **2c** clearly displays metallic behavior, as

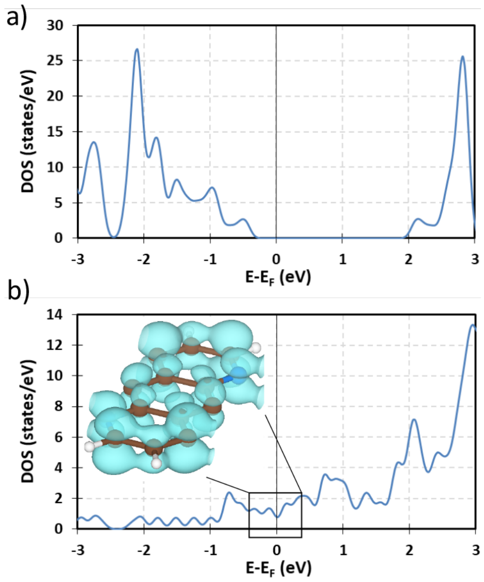

Figure 7. DOS plots calculated at the HSE06 level for (a) fjord-edge GNR **1c** and (b) fully cyclized $N_2[8]_A$GNR **2c**. The inset shows a 3D representation of the partial charge density at the Fermi level in the [−0.2, 0.2] eV range for **2c**.

indicated by the continuous DOS landscape at the Fermi level depicted in Figure 7b. Notice that the HSE06 results are in agreement with the results at the PBE level of theory (Figure S37).[51] Namely, both predict **2c** to be metallic and **1c** to be a semiconductor, although the band gap predicted by PBE is smaller than by HSE06 (1.43 eV vs 2.04 eV, respectively), as expected from the DFT delocalization error.[70] Furthermore, bond-equalization of many of the carbon−carbon bonds within the structure of fully fused $N_2[8]_A$GNR **2c**, unlike those in fjord edge structure **1c** (Figure S38),[51] indicates that $N_2[8]_A$GNR **2c** has quinoid character, which incites its metallic nature. This fact is in agreement with the charge density at the Fermi level, which exhibits a delocalized π-character (Figure 7b, inset).

These calculations indicate that experimental isolation of the fully cyclized, metallic $N_2[8]_A$GNRs **2a,b** could be challenging, and despite our best efforts so far, this step is awaiting further work. Formation and characterization of these novel, exciting graphene nanoribbons is currently under investigation.

CONCLUSION

In summary, we have demonstrated the synthesis of a novel fjord-edge $N_2[8]$GNR system with site-specific nitrogen substitution. The stepwise conversion from dipyridyl diynes **3a,b** to the nitrogen doped, fjord edge $N_2[8]$GNRs **1a,b** via topochemical polymerization of PDAs **4a,b**, followed by Hopf cyclizations to the GNRs, proceeded at relatively moderate temperatures of 330−360 °C. The formation of the fjord-edge structure in the GNRs **1a,b** was confirmed via CP/MAS ^{13}C NMR, XPS, and Raman spectroscopy. The success of our bottom-up method demonstrates the versatility of the crystalline state topochemical polymerization method to incorporate heteroatom substitution and structural diversity into GNR structures.

ASSOCIATED CONTENT

Supporting Information

The Supporting Information is available free of charge at https://pubs.acs.org/doi/10.1021/jacs.0c07657.

Experimental procedures and spectroscopic characterization data, crystallization procedures, HR-TEM imaging, and details of the DFT and Molecular Mechanics calculations (PDF)

Crystallographic data (CIF)

AUTHOR INFORMATION

Corresponding Author

Yves Rubin − *Department of Chemistry and Biochemistry, University of California, Los Angeles, Los Angeles, California 90095−1567, United States;* orcid.org/0000-0003-0187-9689; Email: rubin@chem.ucla.edu

Authors

Yolanda L. Li − *Department of Chemistry and Biochemistry, University of California, Los Angeles, Los Angeles, California 90095−1567, United States;* orcid.org/0000-0002-2180-3086

Chih-Te Zee − *Department of Chemistry and Biochemistry, University of California, Los Angeles, Los Angeles, California 90095−1567, United States*

Janice B. Lin − *Department of Chemistry and Biochemistry, University of California, Los Angeles, Los Angeles, California 90095−1567, United States;* orcid.org/0000-0002-9333-5760

Victoria M. Basile − *Department of Chemistry and Biochemistry, University of California, Los Angeles, Los Angeles, California 90095−1567, United States*

Mit Muni − *Department of Chemistry and Biochemistry, University of California, Los Angeles, Los Angeles, California 90095−1567, United States*

Maria D. Flores − *Department of Chemistry and Biochemistry, University of California, Los Angeles, Los Angeles, California 90095−1567, United States*

Julen Munárriz − *Department of Chemistry and Biochemistry, University of California, Los Angeles, Los Angeles, California 90095−1567, United States;* orcid.org/0000-0001-6089-6126

Richard B. Kaner − *Department of Chemistry and Biochemistry, University of California, Los Angeles, Los Angeles, California 90095−1567, United States;* orcid.org/0000-0003-0345-4924

Anastassia N. Alexandrova − *Department of Chemistry and Biochemistry, University of California, Los Angeles, Los Angeles, California 90095−1567, United States;* orcid.org/0000-0002-3003-1911

K. N. Houk − *Department of Chemistry and Biochemistry, University of California, Los Angeles, Los Angeles, California 90095−1567, United States;* orcid.org/0000-0002-8387-5261

Sarah H. Tolbert − *Department of Chemistry and Biochemistry, University of California, Los Angeles, Los Angeles, California 90095−1567, United States;* orcid.org/0000-0001-9969-1582

Complete contact information is available at: https://pubs.acs.org/10.1021/jacs.0c07657

Notes

The authors declare no competing financial interest.

■ ACKNOWLEDGMENTS

This work was supported by grants from the National Science Foundation to Y.R. (NSF-CHE-1808836), K.N.H. (NSF-DMR-1335645 and NSF-CHE-1254897), A.N.A. (NSF-CHE-1351968), S.H.T. and Y.R. (NSF-CHE-1608957) and NSF-MRI-1532232. This work used computational and storage services associated with the Hoffman2 cluster provided by the UCLA Institute for Digital Research and Education's Research Technology Group, the NSF-supported Extreme Science and Engineering Discovery Environment (XSEDE) (NSF-OCI−1054575 and TG-CHE160054), and high-performance research computing resources by Texas A&M University (http://hprc.tamu.edu). M.D.F. is funded by a Ruth L. Kirschstein National Research Service Award GM007185 and a National Science Foundation Graduate Research Fellowship. C.-T.Z. is funded by a George Gregory Fellowship. R.B.K. thanks the Dr. Myung Ki Hong Chair in Materials Innovation. Data collection at the Argonne National Lab was funded by DOE grant no. DE-FC02-02ER63421. We thank Drs. Duilio Cascio and Michael R. Sawaya for organizing the single crystal data collection at the Advanced Photon Source of Argonne National Laboratory, Dr. Ta-Chung Ong and Dr. Robert Taylor for their assistance with the CP/MAS NMR experiments, and Prof. Jose A. Rodriguez for advice and assistance with the crystal data collection and structure analysis.

■ REFERENCES

(1) Zhou, X.; Yu, G. Modified Engineering of Graphene Nanoribbons Prepared via On-Surface Synthesis. *Adv. Mater.* **2020**, *32*, 1905957.

(2) Llinas, J. P.; Fairbrother, A.; Barin, G. B.; Shi, W.; Lee, K.; Wu, S.; Choi, B. Y.; Braganza, R.; Lear, J.; Kau, N.; Choi, W.; Chen, C.; Pedramrazi, Z.; Dumslaff, T.; Narita, A.; Feng, X.; Müllen, K.; Fischer, F.; Zettl, A.; Ruffieux, P.; Yablonovitch, E.; Crommie, M.; Fasel, R.; Bokor, J. Short-Channel Field-Effect Transistors with 9-Atom and 13-Atom Wide Graphene Nanoribbons. *Nat. Commun.* **2017**, *8*, 633.

(3) Li, X.; Wang, X.; Zhang, L.; Lee, S.; Dai, H. Chemically Derived, Ultrasmooth Graphene Nanoribbon Semiconductors. *Science* **2008**, *319*, 1229−1232.

(4) Shen, H.; Shi, Y.; Wang, X. Synthesis, Charge Transport and Device Applications of Graphene Nanoribbons. *Synth. Met.* **2015**, *210*, 109−122.

(5) Rajaji, U.; Arumugam, R.; Chen, S.-M.; Chen, T.-W.; Tseng, T.-W.; Chinnapaiyan, S.; Lee, S.-Y.; Chang, W.-H. Graphene Nanoribbons in Electrochemical Sensors and Biosensors: A Review. *Int. J. Electrochem. Sci.* **2018**, *13*, 6643−6654.

(6) Cho, K. M.; Cho, S.-Y.; Chong, S.; Koh, H.-J.; Kim, D. W.; Kim, J.; Jung, H.-T. Edge-Functionalized Graphene Nanoribbon Chemical Sensor: Comparison with Carbon Nanotube and Graphene. *ACS Appl. Mater. Interfaces* **2018**, *10*, 42905−42914.

(7) Nakada, K.; Fujita, M.; Dresselhaus, G.; Dresselhaus, M. S. Edge State in Graphene Ribbons: Nanometer Size Effect and Edge Shape Dependence. *Phys. Rev. B: Condens. Matter Mater. Phys.* **1996**, *54*, 17954−17961.

(8) Fujita, M.; Wakabayashi, K.; Nakada, K.; Kusakabe, K. Peculiar Localized State at Zigzag Graphite Edge. *J. Phys. Soc. Jpn.* **1996**, *65*, 1920−1923.

(9) Hao, Z.; Zhang, H.; Ruan, Z.; Yan, C.; Lu, J.; Cai, J. Tuning Electronic Properties of Atomically Precise Graphene Nanoribbons by Bottom-up Fabrications. *ChemNanoMat* **2020**, *6*, 493−515.

(10) Wang, X.-Y.; Yao, X.; Müllen, K. Polycyclic Aromatic Hydrocarbons in the Graphene Era. *Sci. China: Chem.* **2019**, *62*, 1099−1144.

(11) Cai, J.; Ruffieux, P.; Jaafar, R.; Bieri, M.; Braun, T.; Blankenburg, S.; Muoth, M.; Seitsonen, A.; Saleh, M.; Feng, X.; Müllen, K.; Fasel, R. Atomically Precise Bottom-up Fabrication of Graphene Nanoribbons. *Nature* **2010**, *466*, 470−473.

(12) Bronner, C.; Durr, R. A.; Rizzo, D. J.; Lee, Y.-L.; Marangoni, T.; Kalayjian, A. M.; Rodriguez, H.; Zhao, W.; Louie, S. G.; Fischer, F. R.; Crommie, M. F. Hierarchical On-Surface Synthesis of Graphene Nanoribbon Heterojunction. *ACS Nano* **2018**, *12*, 2193−2200.

(13) Beyer, D.; Wang, S.; Pignedoli, C. A.; Melidonie, J.; Yuan, B.; Li, C.; Wilhelm, J.; Ruffieux, P.; Berger, R.; Müllen, K.; Fasel, R.; Feng, X. Graphene Nanoribbons Derived from Zigzag Edge-Encased Poly(para-2,9-dibenzo[bc,kl]coronen-ylene) Polymer Chains. *J. Am. Chem. Soc.* **2019**, *141*, 2843−2846.

(14) Radocea, A.; Sun, T.; Vo, T.; Sinitskii, A.; Aluru, N.; Lyding, J. Solution-Synthesized Chevron Graphene Nanoribbons Exfoliated onto H:Si(100). *Nano Lett.* **2017**, *17*, 170−178.

(15) Gao, J.; Uribe-Romo, F. J.; Saathoff, J. D.; Arslan, H.; Crick, C. R.; Hein, S. J.; Itin, B.; Clancy, P.; Dichtel, W. R.; Loo, Y.-L. Ambipolar Transport in Solution-Synthesized Graphene Nanoribbons. *ACS Nano* **2016**, *10*, 4847−4856.

(16) Li, G.; Yoon, K.-Y.; Zhong, X.; Zhu, X.; Dong, G. Efficient Bottom-Up Preparation of Graphene Nanoribbons by Mild Suzuki−Miyaura Polymerization of Simple Triaryl Monomers. *Chem. - Eur. J.* **2016**, *22*, 9116−9120.

(17) Yang, W.; Lucotti, A.; Tommasini, M.; Chalifoux, W. A. Bottom-Up Synthesis of Soluble and Narrow Graphene Nanoribbons Using Alkyne Benzannulations. *J. Am. Chem. Soc.* **2016**, *138*, 9137−9144.

(18) Hayashi, H.; Yamaguchi, J.; Jippo, H.; Hayashi, R.; Aratani, N.; Ohfuchi, M.; Sato, S.; Yamada, H. Experimental and Theoretical Investigations of Surface-Assisted Graphene Nanoribbon Synthesis Featuring Carbon-Fluorine Bond Cleavage. *ACS Nano* **2017**, *11*, 6204−6210.

(19) Di Giovannantonio, M.; Deniz, O.; Urgel, J. I.; Widmer, R.; Dienel, T.; Stolz, S.; Sánchez-Sánchez, C.; Muntwiler, M.; Dumslaff, T.; Berger, R.; Narita, A.; Feng, X.; Müllen, K.; Ruffieux, P.; Fasel, R. On-Surface Growth Dynamics of Graphene Nanoribbons: The Role of Halogen Functionalization. *ACS Nano* **2018**, *12*, 74−81.

(20) Kolmer, M.; Steiner, A. K.; Izydorczyk, I.; Ko, W.; Engelund, M.; Szymonski, M.; Amsharov, K. Rational Synthesis of Atomically Precise Graphene Nanoribbons Directly on Metal Oxide Surfaces. *Science* **2020**, *369*, 571−575.

(21) Ruffieux, P.; Wang, S.; Yang, B.; Sánchez-Sánchez, C.; Liu, J.; Dienel, T.; Talirz, L.; Shinde, P.; Pignedoli, C. A.; Passerone, D.; Dumslaff, T.; Feng, X.; Müllen, K.; Fasel, R. On-Surface Synthesis of Graphene Nanoribbons with Zigzag Edge Topology. *Nature* **2016**, *531*, 489−492.

(22) Lee, Y.-L.; Zhao, F.; Cao, T.; Ihm, J.; Louie, S. G. Topological Phases in Cove-Edged and Chevron Graphene Nanoribbons: Geometric Structures, z2 Invariants, and Junction States. *Nano Lett.* **2018**, *18*, 7247−7253.

(23) Teeter, J. D.; Costa, P. S.; Pour, M. M.; Miller, D. P.; Zurek, E.; Enders, A.; Sinitskii, A. Epitaxial Growth of Aligned Atomically Precise Chevron Graphene Nanoribbons on Cu(111). *Chem. Commun.* **2017**, *53*, 8463−8466.

(24) Bronner, C.; Stremlau, S.; Gille, M.; Brauße, F.; Haase, A.; Hecht, S.; Tegeder, P. Aligning the Band Gap of Graphene Nanoribbons by Monomer Doping. *Angew. Chem., Int. Ed.* **2013**, *52*, 4422−4425.

(25) Liu, J.; Li, B.-W.; Tan, Y.-Z.; Giannakopoulos, A.; Sánchez-Sánchez, C.; Beljonne, C.; Ruffieux, P.; Fasel, R.; Feng, X.; Müllen, K. Toward Cove-Edged Low Band Gap Graphene Nanoribbons. *J. Am. Chem. Soc.* **2015**, *137*, 6097−6103.

(26) Verzhbitskiy, I. A.; De Corato, M.; Ruini, A.; Molinari, E.; Narita, A.; Hu, Y.; Schwab, M. G.; Bruna, M.; Yoon, D.; Milana, S.; Feng, X.; Müllen, K.; Ferrari, A. C.; Casiraghi, C.; Prezzi, D. Raman

Fingerprints of Atomically Precise Graphene Nanoribbons. *Nano Lett.* **2016**, *16*, 3442−3447.

(27) Wu, J.; Gu, Y.; Muñoz-Mármol, R.; Wu, S.; Han, Y.; Ni, Y.; Díaz-García, M.; Casado, J. Cove-Edged Nanographenes with Localized Double Bonds. *Angew. Chem., Int. Ed.* **2020**, *59*, 8113−8117.

(28) Yano, Y.; Mitoma, N.; Matsushima, K.; Wang, F.; Matsui, K.; Takakura, A.; Miyauchi, Y.; Ito, H.; Itami, K. Living Annulative π-Extension Polymerization for Graphene Nanoribbon Synthesis. *Nature* **2019**, *571*, 387−392.

(29) Moreno, C.; Vilas-Varela, M.; Kretz, B.; Garcia-Lekue, A.; Costache, M. V.; Paradinas, M.; Panighel, M.; Ceballos, G.; Valenzuela, S. O.; Peña, D.; Mugarza, A. Bottom-up Synthesis of Multifunctional Nanoporous Graphene. *Science* **2018**, *360*, 199−203.

(30) Pawlak, R.; Liu, X.; Ninova, S.; D'Astolfo, P.; Drechsel, C.; Sangtarash, S.; Häner, R.; Decurtins, S.; Sadeghi, H.; Lambert, C. J.; Aschauer, U.; Liu, S.-X.; Meyer, E. Bottom-up Synthesis of Nitrogen-Doped Porous Graphene Nanoribbons. *J. Am. Chem. Soc.* **2020**, *142*, 12568−12573.

(31) Jacobse, P. H.; McCurdy, R. D.; Jiang, J.; Rizzo, D. J.; Veber, G.; Butler, P.; Zuzak, R.ł; Louie, S. G.; Fischer, F. R.; Crommie, M. F. Bottom-up Assembly of Nanoporous Graphene with Emergent Electronic States. *J. Am. Chem. Soc.* **2020**, *142*, 13507−13514.

(32) Wang, X.-Y.; Yao, X.; Narita, A.; Müllen, K. Heteroatom-Doped Nanographenes with Structural Precision. *Acc. Chem. Res.* **2019**, *52*, 2491−2505.

(33) Kawai, S.; Saito, S.; Osumi, S.; Yamaguchi, S.; Foster, A. S.; Spijker, P.; Meyer, E. Atomically Controlled Substitutional Boron-Doping of Graphene Nanoribbons. *Nat. Commun.* **2015**, *6*, 8098.

(34) Wang, X.-Y.; Urgel, J. I.; Barin, G. B.; Eimre, K.; Di Giovannantonio, M.; Milani, A.; Tommasini, M.; Pignedoli, C. A.; Ruffieux, P.; Feng, X.; Fasel, R.; Müllen, K.; Narita, A. Bottom-Up Synthesis of Heteroatom-Doped Chiral Graphene Nanoribbons. *J. Am. Chem. Soc.* **2018**, *140*, 9104−9107.

(35) Cao, Y.; Qi, J.; Zhang, Y.-F.; Huang, L.; Zheng, Q.; Lin, X.; Cheng, Z.; Zhang, Y.-Y.; Feng, X.; Du, S.; Pantelides, S. T.; Gao, H.-J. Tuning the Morphology of Chevron-Type Graphene Nanoribbons by Choice of Annealing Temperature. *Nano Res.* **2018**, *11*, 6190−6196.

(36) Nguyen, G. D.; Toma, F. M.; Cao, T.; Pedramrazi, Z.; Chen, C.; Rizzo, D. J.; Joshi, T.; Bronner, C.; Chen, Y.-C.; Favaro, M.; Louie, S. G.; Fischer, F. R.; Crommie, M. F. Bottom-Up Synthesis of N = 13 Sulfur-Doped Graphene Nanoribbons. *J. Phys. Chem. C* **2016**, *120*, 2684−2687.

(37) Kim, K. T.; Lee, J. W.; Jo, W. H. Charge-Transport Tuning of Solution-Processable Graphene Nanoribbons by Substitutional Nitrogen Doping. *Macromol. Chem. Phys.* **2013**, *214*, 2768−2773.

(38) Vo, T. H.; Perera, U. G. E.; Shekhirev, M.; Pour, M. M.; Kunkel, D. A.; Lu, H.; Gruberman, A.; Sutter, E.; Cotlet, M.; Nykypanchuk, D.; Zahl, P.; Enders, A.; Sinitskii, A.; Sutter, P. Nitrogen-Doping Induced Self-Assembly of Graphene Nanoribbon-Based Two-Dimensional and Three-Dimensional Metamaterials. *Nano Lett.* **2015**, *15*, 5770−5777.

(39) Kawai, S.; Nakatsuka, S.; Hatakeyama, T.; Pawlak, R.; Meier, T.; Tracey, J.; Meyer, E.; Foster, A. S. Multiple Heteroatom Substitution to Graphene Nanoribbon. *Science Advances* **2018**, *4*, eaar7181.

(40) Cloke, R. R.; Marangoni, T.; Nguyen, G. D.; Joshi, T.; Rizzo, D. J.; Bronner, C.; Cao, T.; Louie, S. G.; Crommie, M. F.; Fischer, F. R. Site-Specific Substitutional Boron Doping of Semiconducting Armchair Graphene Nanoribbons. *J. Am. Chem. Soc.* **2015**, *137*, 8872−8875.

(41) Piskun, I.; Blackwell, R.; Jornet-Somoza, J.; Zhao, F.; Rubio, A.; Louie, S.; Fischer, F. Covalent C-N Bond Formation through a Surface Catalyzed Thermal Cyclodehydrogenation. *J. Am. Chem. Soc.* **2020**, *142*, 3696−3700.

(42) Cai, J.; Pignedoli, C. A.; Talirz, L.; Ruffieux, P.; Sode, H.; Liang, L.; Meunier, V.; Berger, R.; Li, R.; Feng, X.; Müllen, K.; Fasel, R. Graphene Nanoribbon Heterojunctions. *Nat. Nanotechnol.* **2014**, *9*, 896−900.

(43) Zhang, Y.; Zhang, Y.; Li, G.; Lu, J.; Lin, X.; Du, S.; Berger, R.; Feng, X.; Müllen, K.; Gao, H.-J. Direct Visualization of Atomically Precise Nitrogen-Doped Graphene Nanoribbons. *Appl. Phys. Lett.* **2014**, *105*, No. 023101.

(44) Durr, R. A.; Haberer, D.; Lee, Y.-L.; Blackwell, R.; Kalayjian, A. M.; Marangoni, T.; Ihm, J.; Louie, S. G.; Fischer, F. R. Orbitally Matched Edge-Doping in Graphene Nanoribbons. *J. Am. Chem. Soc.* **2018**, *140*, 807−813.

(45) Vo, T. H.; Shekhirev, M.; Kunkel, D. A.; Orange, F.; Guinel, M. F.-F.; Enders, A.; Sinitskii, A. Bottom-Up Solution Synthesis of Narrow Nitrogen-Doped Graphene Nanoribbons. *Chem. Commun.* **2014**, *50*, 4172−4174.

(46) Wegner, G. Topochemical Polymerization of Monomers with Conjugated Triple Bonds. *Makromol. Chem.* **1972**, *154*, 35−48.

(47) Enkelmann, V. (1984) Structural aspects of the topochemical polymerization of diacetylenes. In: Cantow, H. J. (eds) *Polydiacetylenes. Advances in Polymer Science*, vol 63. Springer: Berlin, Heidelberg, DOI: 10.1007/BFb0017652.

(48) Lauher, J.; Fowler, F.; Goroff, N. Single-Crystal-to-Single-Crystal Topochemical Polymerizations by Design. *Acc. Chem. Res.* **2008**, *41*, 1215−1229.

(49) Jordan, R. S.; Wang, Y.; McCurdy, R. D.; Yeung, M. T.; Marsh, K. L.; Kahn, S. I.; Kaner, R. B.; Rubin, Y. Synthesis of Graphene Nanoribbons via the Topochemical Polymerization and Subsequent Aromatization of a Diacetylene Precursor. *Chem.* **2016**, *1*, 78−90.

(50) Jordan, R. S.; Li, Y. L.; Lin, C.-W.; McCurdy, R. D.; Lin, J. B.; Brosmer, J. L.; Marsh, K. L.; Khan, S. I.; Houk, K. N.; Kaner, R. B.; Rubin, Y. Synthesis of *N* = 8 Armchair Graphene Nanoribbons from Four Distinct Polydiacetylenes. *J. Am. Chem. Soc.* **2017**, *139*, 15878−15890.

(51) See Supporting Information.

(52) See reference 49 for a similar observation on an intermediate stage to $[8]_A$GNR.

(53) Ryu, S.; Maultzsch, J.; Han, M. Y.; Kim, P.; Brus, L. E. Raman Spectroscopy of Lithographically Patterned Graphene Nanoribbons. *ACS Nano* **2011**, *5*, 4123−4130.

(54) Ortiz-Medina, J.; García-Betancourt, M. L.; Jia, X.; Martínez-Gordillo, R.; Pelagio-Flores, M. A.; Swandon, D.; Elías, A. L.; Gutiérrez, H. R.; Garcia-Espino, E.; Meunier, V.; Owens, J.; Sumpter, B. G.; Cruz-Silva, E.; Rodríguez-Macías, F. J.; López-Urías, F.; Muñoz-Sandoval, E.; Dresselhaus, M. S.; Terrones, H.; Terrones, M. Nitrogen-Doped Graphitic Nanoribbons:Synthesis, Characterization, and Transport. *Adv. Funct. Mater.* **2013**, *23*, 3755−3762.

(55) Daigle, M.; Maio, D.; Lucotti, A.; Tommasini, M.; Morin, J.-F. Helically Coiled Graphene Nanoribbons. *Angew. Chem.* **2017**, *129*, 6309−6313.

(56) Zhang, C.; Fu, L.; Liu, N.; Lui, M.; Wang, Y.; Liu, Z. Synthesis of Nitrogen-Doped Graphene Using Embedded Carbon and Nitrogen Sources. *Adv. Mater.* **2011**, *23*, 1020−1024.

(57) Lu, Y.-F.; Lo, S.-T.; Lin, J.-C.; Zhang, W.; Lu, J.-Y.; Liu, F.-H.; Tseng, C.-M.; Lee, Y.-H.; Liang, C.-T.; Li, L.-L. Nitrogen-Doped Graphene Sheets Grown by Chemical Vapor Deposition: Synthesis and Influence of Notrogen Impurities on Carrier Transport. *ACS Nano* **2013**, *7*, 6522−6532.

(58) Liu, M.; Song, Y.; He, S.; Tjiu, W. W.; Pan, J.; Xia, Y.-Y.; Liu, T. Nitrogen-Doped Graphene Nanoribbons as Efficient Metal-Free Electrocatalysts for Oxygen Reduction. *ACS Appl. Mater. Interfaces* **2014**, *6*, 4212−4222.

(59) Wang, G.; Maiyalagan, T.; Wang, X. Review on Recent Progress in Nitrogen-Doped Graphene: Synthesis, Characterization, and Its Potential Applications. *ACS Catal.* **2012**, *2*, 781−794.

(60) Geng, J.; Si, L.; Guo, H.; Lin, C.; Xi, Y.; Li, Y.; Yan, X.; Wang, B.; Chen, L. 3D Nitrogen-Doped Graphene Gels as Robust and Sustainable Adsorbents for Dyes. *New J. Chem.* **2017**, *41*, 15447−15457.

(61) Kondo, T.; Casolo, S.; Suzuki, T.; Shikano, T.; Sakurai, M.; Harada, Y.; Saito, M.; Oshima, M.; Trioni, M. I.; Tantardini, G. F.; Nakamura, J. Atomic-Scale Characterization of Nitrogen-Doped Graphite: Effects of Dopant Nitrogen on the Local Electronic

Structure of the Surrounding Carbon Atoms. *Phys. Rev. B: Condens. Matter Mater. Phys.* **2012**, *86*, No. 035436.

(62) Jansen, R. J. J.; van Bekkum, H. XPS of Nitrogen-Containing Functional Groups on Activated Carbon. *Carbon* **1995**, *8*, 1021−1027.

(63) Tian, Z.; Dai, S.; Jiang, D. Stability and Core-Level Signature of Nitrogen Dopants in Carbonaceous Materials. *Chem. Mater.* **2015**, *27*, 5775−5781.

(64) Kapteijn, F.; Moulijn, J. A.; Matzner, S.; Boehm, H.-P. The Development of Nitrogen Functionality in Model Chars during Gasification in CO2 and O2. *Carbon* **1999**, *37*, 1143−1150.

(65) Matanovic, I.; Artyushkova, K.; Strand, M. B.; Dzara, M. J.; Pylypenko, S.; Atanassov, P. Core Level Shifts of Hydrogenated Pyridinic and Pyrrolic Nitrogen in the Nitrogen-Containing Graphene-Based Electrocatalysts: In-Place vs Edge Defects. *J. Phys. Chem. C* **2016**, *120*, 29225−29232.

(66) Men, S.; Mitchell, D. S.; Lovelock, K. R. J.; License, P. X-ray Photoelectron Spectroscopy of Pyridinium-Based Ionic Liquids: Comparison to Imidazolium- and Pyrrolidinium-Based Analogues. *ChemPhysChem* **2015**, *16*, 2211−2218.

(67) Prall, M.; Krüger, A.; Schreiner, P. R.; Hopf, H. The Cyclization of Parent and Cyclic Hexa-1,3-dien-5-ynes—A Combined Theoretical and Experimental Study. *Chem. - Eur. J.* **2001**, *7*, 4386−4394.

(68) Krukau, A. V.; Vydrov, O. A.; Izmaylov, A. F.; Scuseria, G. E. Influence of the exchange screening parameter on the performance of screened hybrid functionals. *J. Chem. Phys.* **2006**, *125*, 224106.

(69) Perdew, J. P.; Burke, K.; Ernzerhof, M. Generalized Gradient Approximation Made Simple. *Phys. Rev. Lett.* **1996**, *77*, 3865−3868.

(70) Mori-Sanchez, P.; Cohen, A. J.; Yang, W. Localization and Delocalization Errors in Density Functional Theory and Implications for Band-Gap Prediction. *Phys. Rev. Lett.* **2008**, *100*, 146401.